PLC-C: An Integrated Method for Sentinel-2 Topographic and Angular Normalization

Gaofei Yin, *Member, IEEE*, Jing Li, Baodong Xu, Yelu Zeng, Shengbiao Wu, Kai Yan, Aleixandre Verger, and Guoxiang Liu

***Abstract*— Topographic and angular corrections on Sentinel-2 imagery are crucial for the generation of consistent surface reflectance. We propose a novel topographic-angular integrated normalization approach based on the combination of the path length correction (PLC) and C-factor approaches. The PLC-C normalization approach is a semiphysical method with limited use of auxiliary data: only a digital elevation model and a fixed set of kernel coefficients, ensuring its transferability for operational implementation. For the validation, we used two Sentinel-2A images over a mountainous area observed in backward (BS) and forward scattering (FS) directions from laterally adjacent orbit swaths. PLC-C significantly reduced both the topographic and directional anisotropy effects: the overlapping ratio between BS and FS observations was increased from 84.1% to 92.8% for the near-infrared band, and from 81.0% to 93.1% for the red band; the coefficient of variation of the reflectances across different aspects, which was used as a criterion of topographic effects, was reduced from 9.8% / 12.2% to 3.6%/5.7% in BS/FS direction for the near-infrared band, and from 8.1%/9.7% to 4.5%/4.2% for the red band. PLC-C will contribute to the generation of analysis ready data from Sentinel-2 top of canopy reflectance.**

***Index Terms*— Angular normalization, bidirectional reflectance distribution function (BRDF), consistent surface reflectance, Sentinel-2, topographic normalization.**

Manuscript received January 13, 2020; revised May 4, 2020 and June 6, 2020; accepted June 9, 2020. Date of publication June 19, 2020; date of current version July 22, 2021. This work was supported in part by the National Natural Science Foundation of China under Grant 41971282, in part by the GF6 Project under Grant 30-Y20A03-9003-17/18, in part by the Youth Innovation Promotion Association Chinese Academy of Sciences (CAS) under Grant 2016333, and in part by the European Union's Horizon 2020 research and innovation program the Marie Skłodowska-Curie under Grant 835541 *(Corresponding author: Gaofei Yin.)*

Gaofei Yin is with the Faculty of Geosciences and Environmental Engineering, Southwest Jiaotong University, Chengdu 610031, China, also with the CREAF, 08193 Cerdanyola del Vallès, Spain, and also with the CSIC, Global Ecology Unit, 08193 Cerdanyola del Vallès, Spain (e-mail: yingf@swjtu.edu.cn).

Jing Li and Shengbiao Wu are with the State Key Laboratory of Remote Sensing Science, Institute of Remote Sensing and Digital Earth, Chinese Academy of Sciences, Beijing 100101, China.

Baodong Xu is with the Macro Agriculture Research Institute, College of Resources and Environment, Huazhong Agricultural University, Wuhan 430070, China.

Yelu Zeng is with the Department of Global Ecology, Carnegie Institution for Science, Stanford, CA 94305 USA.

Kai Yan is with the School of Land Science and Techniques, China University of Geosciences, Beijing 100083, China.

Aleixandre Verger is with the CREAF, 08193 Cerdanyola del Vallès, Spain, and also with the CSIC, Global Ecology Unit, 08193 Cerdanyola del Vallès, Spain.

Guoxiang Liu is with the Faculty of Geosciences and Environmental Engineering, Southwest Jiaotong University, Chengdu 610031, China.

Color versions of one or more of the figures in this letter are available online at https://ieeexplore.ieee.org.

Digital Object Identifier 10.1109/LGRS.2020.3001905

I. Introduction

Sentinel-2 mission delivers surface reflectance measurements in 13 spectral channels in the visible, near-infrared, and shortwave infrared domains, at high spatial resolution (10–20–60 m) and revisit frequency (five days in tandem) [1]. The free access policy and the high quality of the data highly benefit many land surface applications. However, many confounding factors, including solar and viewing geometry anisotropy, and topography, introduce uncertainty in the retrieval and interpretation of surface intrinsic reflectance for downstream applications [2].

Previous studies revealed that Sentinel-2 has nonnegligible directional anisotropic effects [3], [4]. These angular effects can be successfully reduced through the application of a kernel-driven model of the bidirectional reflectance distribution function (BRDF) [5] with kernel coefficients extracted from Moderate Resolution Imaging Spectroradiometer (MODIS) BRDF products [6]. Roy *et al.* [3] found that the BRDF shapes of different terrestrial surfaces are sufficiently similar over the Sentinel-2 field of view (FOV), and a fixed set of kernel coefficients is adequate for angular normalization. This approach was named as C-factor approach and has been widely used for Sentinel-2 imagery [3], [4], [7].

Topographic normalization is also a well-developed research field [8], [9]. Many topographic normalization approaches have been proposed, which can be roughly classified into two main categories: empirical and physical approaches. The former rely on the empirical relationship between reflectance and topographic factors [10], [11]. The latter are generally based on the simplification of physical laws underlying the canopy reflectance models [12]–[14], without any empirical parameter. Validation exercises revealed that the path length correction (PLC) approach, which we proposed in our previous work [13], outperforms other approaches, especially for sensors with a relatively wide FOV such as Sentinel-2 (∼290 km FOV).

The objective of this letter is to propose an integrated topographic and angular normalization for Sentinel-2 reflectances. The method (hereafter referred to as PLC-C) is based on the combination of PLC and C-factor approaches. There is no empirical regression process and limited use of auxiliary data: only a digital elevation model (DEM) and a fixed set of kernel coefficients to characterize the topography and reflectance anisotropy, respectively, which ensures the transferability for operational applications. The proposed approach was validated in a dedicatedly designed experiment.

II. Normalization Method

A. PLC Topographic Normalization Approach

The PLC approach was based on the parametrization of path length, that is, the distance between the top and the bottom of the canopy along a direction, which is a key variable influencing the canopy radiative transfer process and is sensitive to topography [14]. Based on a simplification of the canopy radiative transfer equation, the topographically normalized reflectance (ρ_{TN}) can be obtained from the original reflectance (ρ_{O}) multiplied by a topographic normalization conversion factor (P) [13]

$$\begin{aligned} \rho_{\mathrm{TN}} &= P \times \rho_O \\ P &= \frac{S(\Omega_1) + S(\Omega_2)}{S_t(\Omega_1) + S_t(\Omega_2)} \end{aligned} \tag{1}$$

where $S(\Omega_1)$ and $S(\Omega_2)$ are path lengths along the solar (Ω_1) and viewing (Ω_2) directions, respectively, over the flat terrain, and $S_t(\Omega_1)$ and $S_t(\Omega_2)$ are their counterparts over the sloping terrain. $S(\Omega_1)$ and $S(\Omega_2)$ can simply be calculated as

$$S(\theta) = 1/\cos\theta \tag{2}$$

and $S_t(\Omega_1)$ and $S_t(\Omega_2)$ can be calculated as

$$S_t(\theta, \varphi, \alpha, \beta) = \frac{1}{\cos\theta(1 - \tan\alpha\cos(\varphi - \beta)\tan\theta)}. \tag{3}$$

In (2) and (3), θ and φ are, respectively, the zenith and azimuth angles for the solar or viewing direction, and α and β are, respectively, the slope and aspect for the sloping surface.

B. C-Factor Angular Normalization Approach

Similar to PLC, the C-factor approach can normalize the reflectance from its original angular geometry (ρ_{O}) to the targeted solar and viewing geometries (ρ_{AN}) through an angular normalization conversion factor (C) [3], [15]

$$\begin{aligned} \rho_{\mathrm{AN}} &= C \times \rho_{\mathrm{O}} \\ C &= \tilde{\rho}_{\mathrm{AN}}/\tilde{\rho}_{\mathrm{O}} \end{aligned} \tag{4}$$

where $\tilde{\rho}_{\mathrm{AN}}$ and $\tilde{\rho}_{\mathrm{O}}$ are reflectance at targeted and original solar and viewing geometries estimated from the BRDF kernel-driven model, which can be expressed as [5]

$$\tilde{\rho}(\Omega_1, \Omega_2) = f_{\mathrm{iso}} + f_{\mathrm{vol}} K_{\mathrm{vol}}(\Omega_1, \Omega_2) + f_{\mathrm{geo}} K_{\mathrm{geo}}(\Omega_1, \Omega_2) \tag{5}$$

where $K_{\mathrm{vol}}(\Omega_1, \Omega_2)$ and $K_{\mathrm{geo}}(\Omega_1, \Omega_2)$ are the volumetric scattering and geometric optical kernels, respectively, and f_{iso}, f_{vol}, and f_{geo} are the kernel coefficients. As recommended in [3] and [15], we used the Ross-Thick volumetric scattering and the Li-Sparse geometric optical kernels, and the kernel coefficients proposed by Roy *et al.* [3] for the Sentinel-2A.

C. PLC-C Integrated Topographic-Angular Normalization Approach

The PLC and C-factor approaches, for topographic and angular normalization, respectively, both have a multiplicative form. Based on the assumption that the topographic and angular effects are independent of each other, the integrated normalization can be expressed as

$$\rho_{\mathrm{IN}} = C \times P \times \rho_{\mathrm{O}} \tag{6}$$

where ρ_{O} is the reflectance at the original solar and viewing geometry and suffers from topographic effect, and ρ_{IN} is the topographically normalized reflectance at a targeted solar and viewing geometry, and C and P are the conversion factors for the angular and topographic normalizations, which can be calculated from (1) and (4), respectively,

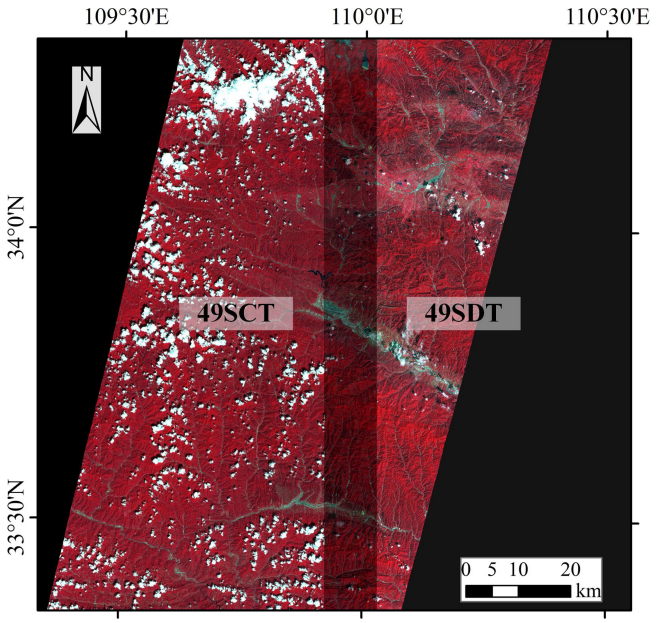

Fig. 1. Sentinel-2A RGB (8, 4, 3) composite of the two laterally adjacent tiles (49SCT and 49SDT) acquired on 24th and 27th of August, 2018, in the BS and FS directions. The shaded area represents the overlapping 10 km × 100 km mountainous area selected to evaluate the proposed topographic and angular normalization method.

III. Experimental Setup

A. Data

Two Sentinel-2A Multispectral Instrument (MSI) Level-1C images collected by laterally adjacent orbit swaths over a mountainous area (see Fig. 1) were downloaded from the Sentinels Scientific Data Hub (https://scihub.copernicus.eu/). Their overlapping area (10 km × 100 km) was sensed twice within three days on 24th and 27th of August, 2018.

Fig. 2 shows the solar-viewing geometries of the two Sentinel-2A images. The solar/viewing zenith angles were very similar: 28.2°/8.6° and 27.8°/9.5° on 24th and 27th August, respectively, but they were observed in backward (BS) and forward scattering (FS) directions close to the solar principal plane where the angular effects are the strongest [3]: relative azimuth angles of 39.9° and 140.8°.

The two Level-1C, that is, top of atmosphere reflectance, Sentinel-2A images were atmospherically corrected using the Sen2Cor processor in the Sentinel Application Platform (SNAP) [16] to obtain top of canopy reflectance, that is, Level-2A. Only the vegetation pixels under clear-sky

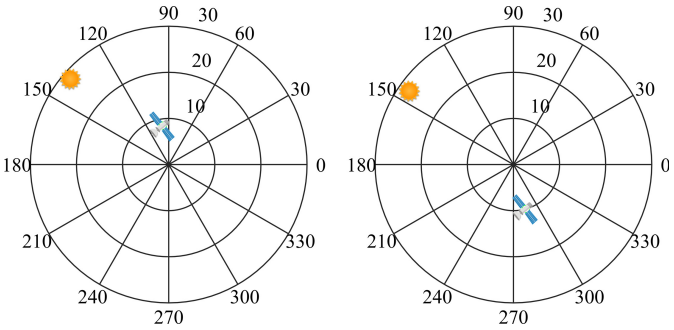

Fig. 2. Polar illustration of the solar and viewing geometry for the selected Sentinel-2A data on 24 (left) and 27 (right) August, 2018, respectively. The polar angle represents the azimuth spaced every 30°, and the radius represents the zenith spaced every 10° with nadir in the center.

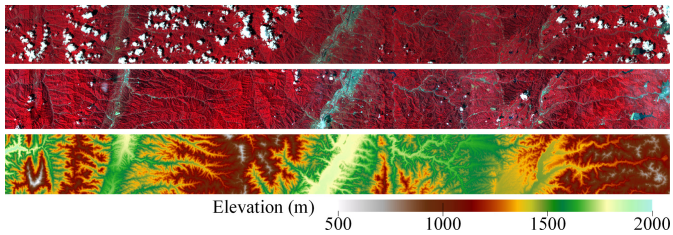

Fig. 3. Sentinel-2A RGB (8, 4, 3) composite of the study area in the BS (top) and FS (middle) directions, and the elevation map (bottom). The original overlapping area (see Fig. 1) was rotated by 90° for illustration purposes.

conditions were selected, that is, cloud and cloud shadows were masked out.

The Advanced Spaceborne Thermal Emission and Reflectance Radiometer (ASTER) Global DEM (GDEM) version 2 product was used for the topographic normalization. It has a resolution of 1" (∼30 m) [17].

Sentinel-2 data were resampled to 30 m to spatially match the ASTER GDEM data (see Fig. 3). The 10 and 20-m bands were up-resampled with the pixel aggregate method in Environment for Visualizing Images (ENVI) that averages all the pixel values that contribute to the output 30-m pixel, and the 60-m bands were down-resampled with the bilinear interpolation method.

B. Evaluation Approach

There are in total 526764 pairs of clear-sky reflectances collected over mountainous (slope > 5°) pixels within three days in the FS and BS directions. These reflectance-pairs were used to evaluate the performance of the proposed topographic and angular correction method. Reflectances were normalized to their equivalent values over a horizontal surface observed in the nadir direction with a solar zenith angle of 28°. All the 13 spectral bands of Sentinel-2 imagery were processed. For brevity, we only show results for the red and near-infrared bands (band 4 centered at 665 and band 8 at 842 nm, respectively), which are widely used for vegetation monitoring.

We propose a novel evaluation method to assess the topographic and angular effects in a common framework. This evaluation method relies on the analysis of reflectance distribution across different aspects. We first calculated the mean reflectance for every aspect, and drew them on a polar plot,

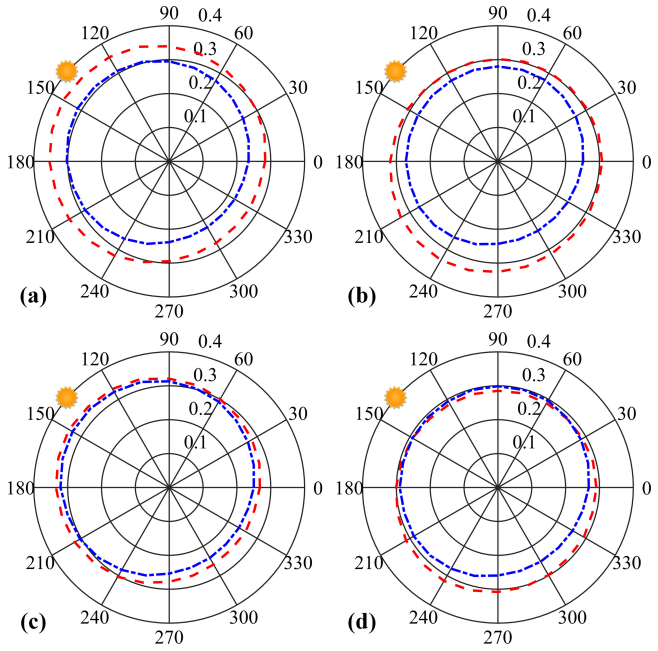

Fig. 4. Mean near-infrared reflectances across aspect angles (a) before normalization, (b) after topographic, (c) angular, and (d) integrated normalization. The red dashed and blue dashed-dot lines represent the BS and FS reflectances, respectively. The radius represents the magnitude of the reflectance with zero in the center, and the polar angle represents the aspect. Solar azimuth (mean value for the two images) was also marked for better representing the topography induced reflectance distortion.

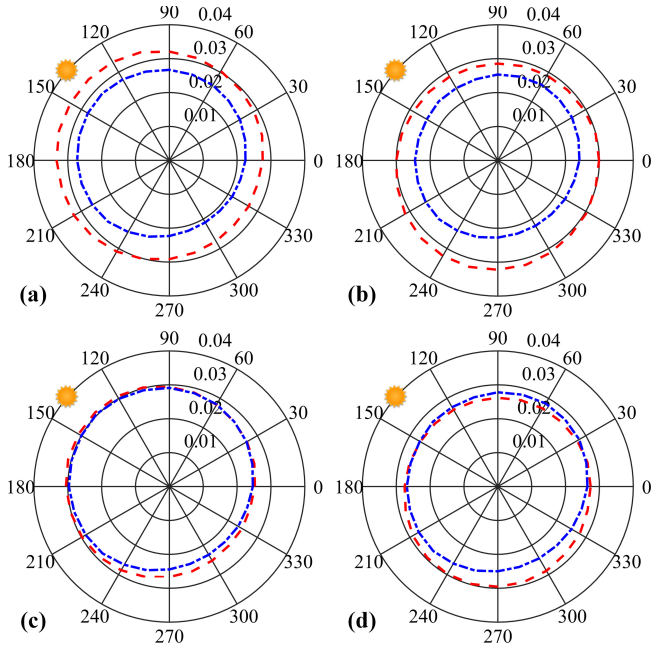

Fig. 5. Same as Fig. 4 but for the red band.

forming an ellipse (see Figs. 4 and 5). The topographic and angular effects on reflectance can both be characterized by analyzing the shape of the ellipse. Topographic effects were separately analyzed for the BS and FS observations, yet angular effect were analyzed by comparing the similarity of the ellipses for the two observation directions.

TABLE I

TOPOGRAPHIC AND ANGULAR EFFECTS IN THE UNNORMALIZED (UN), TOPOGRAPHICALLY NORMALIZED (TN), ANGULARLY NORMALIZED (AN) AND INTEGRATICALLY NORMALIZED (IN) NEAR-INFRARED REFLECTANCES

		UN	TN	AN	IN
Topographic effect	CV_{bs}[(a)]	9.8	3.6	9.9	3.6
	CV_{fs}[(b)]	12.2	5.7	11.9	5.7
Angular effect	OR[(c)]	84.1	83.4	94.5	92.8

(a) Coefficient of variation (%) of backward scattering direction reflectances across different aspects;
(b) Coefficient of variation (%) of forward scattering direction reflectances across different aspects;
(c) Overlapping ratio of the two ellipses for backward scattering and forward scattering reflectances (see Fig. 4).

TABLE II

SAME AS TABLE I BUT FOR THE RED BAND

		UN	TN	AN	IN
Topographic effect	CV_{bs}[(a)]	8.1	4.5	8.2	4.5
	CV_{fs}[(b)]	9.7	4.1	9.3	4.2
Angular effect	OR[(c)]	81.0	80.3	96.1	93.1

Intuitively, topography causes reflectances on the sunny aspects higher than those on the shady aspects. Therefore, reflectances with strong topographic effect will have a very flat ellipse and shift to the solar azimuth. Otherwise, if reflectances are independent of topography, they will form a circle with center located in the origin of the polar coordinate.

For angular effect analysis, the areas of the two ellipses for the BS and FS observations will be quite different if they are characterized by strong reflectance anisotropy. Otherwise, if the angular effect on the two direction observations is successfully normalized, their ellipses will overlap with each other.

Two metrics were used to quantify the topographic and angular effects, respectively: 1) the coefficient of variation (CV) (%) of the reflectances across different aspects was used to quantify the topographic effect; 2) the overlapping ratio (OR) (%) between the intersection of the two ellipses for BS and FS observations was used to quantify the angular effect.

IV. RESULTS

The aspect-distribution of the near-infrared and red reflectances is shown in Figs. 4 and 5, respectively, and the corresponding statistics are listed in Tables I and II.

Before normalization, the ellipse for FS reflectances was fully contained in the BS one, demonstrating that reflectances in BS are systematically larger than FS [Figs. 4(a) and 5(a)] due to the lower proportion of shadows in BS [18]. The systematic bias between BS and FS reflectances resulted in low OR of 84.1% and 81.0% for near-infrared and red bands, respectively. In addition, both the BS and FS reflectances over the sun-facing aspects (around 142.5°) was remarkably larger than those over the opposite directions, revealing obvious topographic effect ($CV_{\mathrm{bs}} = 9.8\%$ and $CV_{\mathrm{fs}} = 12.2\%$ for near-infrared band, and $CV_{\mathrm{bs}} = 8.1\%$ and $CV_{\mathrm{fs}} = 9.7\%$ for red band).

After topographic normalization, the reflectance variations over different aspects were significantly reduced [Figs. 4(b) and 5(b)]. The BS and FS ellipses nearly transformed to circles centered at ordinate origins ($CV_{\mathrm{bs}} = 3.6\%$ and $CV_{\mathrm{fs}} = 5.7\%$ for near-infrared band, and $CV_{\mathrm{bs}} = 4.5\%$ and $CV_{\mathrm{fs}} = 4.1\%$ for red band). The angular effect almost remained the same as the original case: FS ellipse was still contained in the BS one with OR equal to 83.4% and 80.3% for near-infrared and red bands, respectively.

Angular normalization prominently reduced the systematic deviation between the BS and FS reflectances [see Figs. 4(c) and 5(c)]. The vast majority of BS and FS ellipses overlapped each other, and resulted in high OR of 94.5% and 96.1% for the near-infrared and red bands, respectively. Yet the aspect-dependence was still obvious in the BS and FS reflectances for both near-infrared and red bands.

The integrated normalization performed satisfactorily and highly reduced both topographic and angular effects [see Figs. 4(d) and 5(d)]. The capacities of PLC and C-factor approaches in topographic and angular normalizations, respectively, were nearly entirely inherited by the integrated approach: the CV_{bs} and CV_{fs} were nearly the same as the case after PLC normalization, and the OR was similar although slightly lower than the C-factor normalization.

V. DISCUSSION

PLC-C approach assumed that topographic and angular effects are independent of each other. For the red band (cf. Fig. 5 and TABLE II), the OR between BS and FS observations (metrics used to quantify angular effects) were nearly the same before and after topographic normalization (81.0% and 80.3%, respectively). At the same time, the CV for BS/FS observation (metrics for topographic effects) was also nearly the same before and after angular normalization: 8.1%/9.7% and 8.2%/9.3%, respectively. The near-infrared band exhibited similar patterns (cf. Fig. 4 and TABLE I). This means that the topographic normalization would not influence the angular effects, and vice versa, confirming the independence assumption. Many topographic normalization methods apply a simple normalization of sun-target-sensor geometry from horizontal datum to local terrain by coordinate rotation [2], [19], [20]. This treatment violates the geotropic nature of vegetation [13], [14], [21]. In addition, the transformation of topographic normalization to angular normalization makes the definition of sun-target-sensor geometry obscure, undermining the angular normalization in the integrated normalization framework. On the contrary, PLC-C reduces topographic effects from the solution to the classic radiative transfer equation, keeping the original sun-target-sensor geometry of horizontal datum [13], and normalizes angular effects with the C-factor approach.

Residual angular and topographic effects persist in the PLC-C normalized data. The use of uniform kernel coefficients [3] may introduce uncertainties in the angular normalization because different land covers have different BRDF shapes. The residual topographic effects are mainly caused by the assumptions of the PLC approach. To obtain a concise

transformation [see (1)], three main assumptions were made during the simplification of canopy radiative transfer equation: 1) the canopy is illuminated by collimated light; 2) the radiance collected by the sensor is only from the single-scattering of leaves; and 3) the leaf inclination distribution function is spherical [13], [14]. Another explanation of the residual topographic effect is that the reflectances over different aspects are different in reality because of different hydrothermal conditions [22]. Therefore, the residual dependence of reflectance on aspect may conform to the actual situation.

This letter confirmed the high performance of PLC and C-factor approaches in topographic and angular normalizations, and demonstrated the possibility to combine them together to achieve integrated normalization. Further research should focus on two main aspects: 1) This letter combined the topographic and angular normalizations through a simple multiplicative form. Other derivation method of integration normalization operator, such as model simplification, as in [12] and [13], may further improve the physical soundness and (2) the refinement of PLC (e.g., considering the multiscattering) and C-factor approaches (e.g., using more specific kernel coefficients) may further improve the performance of the topographic-angular integrated normalization.

VI. Conclusion

We proposed a novel topographic-angular integrated normalization (PLC-C) for Sentinel-2 based on the combination of PLC and C-factor approaches. The method is based on a physical approach and only uses the free available DEM data and a fixed set of kernel coefficients as auxiliary information, ensuring its transferability for operational implementation. A dedicatedly designed validation experiment showed its high performance for both topographic and angular normalizations. Our approach will contribute to the generation of consistent reflectance and analysis ready data from Sentinel-2 top of canopy reflectance.

Acknowledgment

The authors would like to thank the National Aeronautic and Space Administration and the Ministry of Economy, Trade, and Industry of Japan for making the ASTER GDEM data freely available. The European Space Agency and the EU Copernicus program are also acknowledged for the free delivery of the Sentinel-2A data.

References

[1] N. Lamquin *et al.*, "An inter-comparison exercise of Sentinel-2 radiometric validations assessed by independent expert groups," *Remote Sens. Environ.*, vol. 233, Nov. 2019, Art. no. 111369.

[2] F. Li *et al.*, "A physics-based atmospheric and BRDF correction for Landsat data over mountainous terrain," *Remote Sens. Environ.*, vol. 124, pp. 756–770, Sep. 2012.

[3] D. P. Roy, J. Li, H. K. Zhang, L. Yan, H. Huang, and Z. Li, "Examination of Sentinel-2A multi-spectral instrument (MSI) reflectance anisotropy and the suitability of a general method to normalize MSI reflectance to nadir BRDF adjusted reflectance," *Remote Sens. Environ.*, vol. 199, pp. 25–38, Sep. 2017.

[4] H. K. Zhang *et al.*, "Characterization of Sentinel-2A and Landsat-8 top of atmosphere, surface, and nadir BRDF adjusted reflectance and NDVI differences," *Remote Sens. Environ.*, vol. 215, pp. 482–494, Sep. 2018.

[5] C. B. Schaaf *et al.*, "First operational BRDF, albedo nadir reflectance products from MODIS," *Remote Sens. Environ.*, vol. 83, nos. 1–2, pp. 135–148, Nov. 2002.

[6] B. Franch *et al.*, "A method for Landsat and Sentinel 2 (HLS) BRDF Normalization," *Remote Sens.*, vol. 11, no. 6, p. 632, Mar. 2019.

[7] D. Roy, Z. Li, and H. Zhang, "Adjustment of Sentinel-2 multi-spectral instrument (MSI) red-edge band reflectance to nadir BRDF adjusted reflectance (NBAR) and quantification of red-edge band BRDF effects," *Remote Sens.*, vol. 9, no. 12, p. 1325, Dec. 2017.

[8] D. Riano, E. Chuvieco, J. Salas, and I. Aguado, "Assessment of different topographic corrections in Landsat-TM data for mapping vegetation types (2003)," *IEEE Trans. Geosci. Remote Sens.*, vol. 41, no. 5, pp. 1056–1061, May 2003.

[9] I. Sola, M. González-Audícana, and J. Álvarez-Mozos, "Multi-criteria evaluation of topographic correction methods," *Remote Sens. Environ.*, vol. 184, pp. 247–262, Oct. 2016.

[10] P. M. Teillet, B. Guindon, and D. G. Goodenough, "On the slope-aspect correction of multispectral scanner data," *Can. J. Remote Sens.*, vol. 8, no. 2, pp. 84–106, Dec. 1982.

[11] H. Ge, D. Lu, S. He, A. Xu, G. Zhou, and H. Du, "Pixel-based minnaert correction method for reducing topographic effects on a Landsat 7 ETM+ image," *Photogramm. Eng. Remote Sens.*, vol. 74, no. 11, pp. 1343–1350, Nov. 2008.

[12] J. R. Dymond and J. D. Shepherd, "Correction of the topographic effect in remote sensing," *IEEE Trans. Geosci. Remote Sens.*, vol. 37, no. 5, pp. 2618–2619, Sep. 1999.

[13] G. Yin *et al.*, "PLC: A simple and semi-physical topographic correction method for vegetation canopies based on path length correction," *Remote Sens. Environ.*, vol. 215, pp. 184–198, Sep. 2018.

[14] G. Yin, A. Li, W. Zhao, H. Jin, J. Bian, and S. Wu, "Modeling canopy reflectance over sloping terrain based on path length correction," *IEEE Trans. Geosci. Remote Sens.*, vol. 55, no. 8, pp. 4597–4609, Aug. 2017.

[15] D. P. Roy *et al.*, "A general method to normalize landsat reflectance data to nadir BRDF adjusted reflectance," *Remote Sens. Environ.*, vol. 176, pp. 255–271, Apr. 2016.

[16] J. Louis *et al.*, "Sentinel-2 Sen2Cor: L2A processor for users," in *Proc. Living Planet Symp.*, 2016, pp. 1–8.

[17] T. Tachikawa, M. Hato, M. Kaku, and A. Iwasaki, "Characteristics of ASTER GDEM version 2," in *Proc. IEEE Int. Geosci. Remote Sens. Symp.*, Jul. 2011, pp. 3657–3660.

[18] X. Li and A. H. Strahler, "Geometric-optical bidirectional reflectance modeling of the discrete crown vegetation canopy: Effect of crown shape and mutual shadowing," *IEEE Trans. Geosci. Remote Sens.*, vol. 30, no. 2, pp. 276–292, Mar. 1992.

[19] S. A. Soenen, D. R. Peddle, and C. A. Coburn, "SCS+C: A modified sun-canopy-sensor topographic correction in forested terrain," *IEEE Trans. Geosci. Remote Sens.*, vol. 43, no. 9, pp. 2148–2159, Sep. 2005.

[20] J. Wen *et al.*, "Modeling land surface reflectance coupled BRDF for HJ-1/CCD data of rugged terrain in Heihe River Basin, China," *IEEE J. Sel. Topics Appl. Earth Observ. Remote Sens.*, vol. 8, no. 4, pp. 1506–1518, Apr. 2015.

[21] J. Wen *et al.*, "Characterizing land surface anisotropic reflectance over rugged terrain: A review of concepts and recent developments," *Remote Sens.*, vol. 10, no. 3, p. 370, Feb. 2018.

[22] S. Hantson and E. Chuvieco, "Evaluation of different topographic correction methods for Landsat imagery," *Int. J. Appl. Earth Observ. Geoinf.*, vol. 13, no. 5, pp. 691–700, Oct. 2011.